pubs.acs.org/Biomac

Article

Folic Acid-Modified Cyclodextrin Multivalent Supramolecular Assembly for Photodynamic Therapy

Xianyin Dai, Man Huo, Bing Zhang, Zhixue Liu, and Yu Liu*

Cite This: https://doi.org/10.1021/acs.biomac.2c00276

Read Online

ACCESS | Metrics & More | Article Recommendations | Supporting Information

ABSTRACT: The construction of supramolecular multivalent assemblies with unique photoluminescence behaviors and biological functions has become a research hot spot recently in the biomaterial field. Herein, we report an adaptive supramolecular assembly via a multivalent co-assembly strategy prepared in two stages by using an adamantane-connected pyrenyl pyridinium derivative (APA2), sulfonated aluminum phthalocyanine (PcS), and folic acid-modified β-cyclodextrin (FA−CD) for efficient dual-organelle targeted photodynamic cancer cell ablation. Benefiting from $\pi-\pi$ and electrostatic interactions, APA2 and PcS could first assemble into non-fluorescent irregular nanoaggregates because of the heterodimer aggregation-induced quenching and then secondarily assemble with FA−CD to afford targeted spherical nanoparticles (NPs) with an average diameter of around 50 nm, which could be specifically taken up by HeLa cancer cells through endocytosis in comparison with 293T normal cells. Intriguingly, such multivalent NPs could adaptively disaggregate in an intracellular physiological environment of cancer cells and further respectively and selectively accumulate in mitochondria and lysosomes, which not only displayed near-infrared two-organelle localization in situ but also aroused efficient singlet oxygen generation under light irradiation to effectively eliminate cancer cells up to 99%. This supramolecular multivalent assembly with an adaptive feature in a specific cancer cell environment provides a feasible strategy for precise organelle-targeted imaging and an efficiently synergetic photodynamic effect in situ for cancer cell ablation.

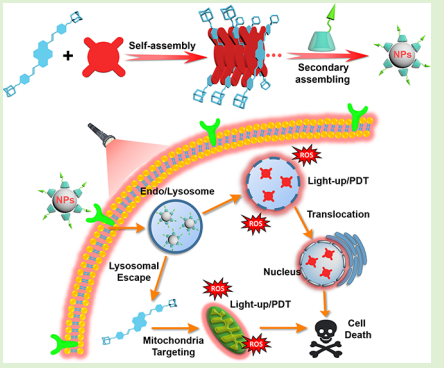

INTRODUCTION

Supramolecular multivalent assemblies based on macrocycles-mediated molecular aggregation or heterodimerization have captured great attention in virtue of their diverse applications such as targeted cell imaging,[1−3] bio-sensing,[4,5] drug delivery,[6,7] and luminescent materials.[8,9] Macrocyclic compounds play a vital role in regulating the molecular assembly process.[10,11] For example, multicharged macrocycles can induce molecules to form assemblies with favorable fluorescence emission and then build artificial light-harvesting or catalytic systems.[12,13] Particularly, photodynamic therapy (PDT) taking advantage of macrocycles-involved multivalent systems has evolved as one of the increasingly striking topics in biological research.[14−16] The introduction of macrocyclic compounds into an assembly can not only alleviate the aggregation of photosensitizers to enhance the reactive oxygen species (ROS) generation ability or modulate the ROS generation on demand through the host−guest interaction[17,18] but also control the self-assembly behavior, which is conducive to improving the efficiency of cell endocytosis.[19,20] Compared with other macrocyclic compounds, cyclodextrin as a kind of macrocyclic molecule with favorable water solubility, low toxicity, and biocompatibility has been conveniently exploited as a fundamental building block to construct multifunctional and advanced supramolecular assemblies.[21−23] For example, cyclodextrin can prompt the formation of highly ordered structures and prevent the accumulation of porphyrins, thus leading to more singlet oxygen generation.[24] Cyclodextrin-based supramolecular systems have also been elaborately applied in organelle dysfunction and cancer therapy.[25−27]

The avoidance the undesired photosensitizer activation is of great significance in the PDT process, which required the photosensitizer to only be initiated in specific sites of cells when meeting a variety of intracellular stimuli.[28−32] Molecules with intramolecular rotation properties such as tetraphenylethene (TPE) derivatives will undergo a remarkable enhancement of fluorescence or ROS generation after aggregation, while most of the molecules are quenched.[33−35] Phthalocyanine derivatives that hold an extended conjugated structure have been widely exploited as photosensitizers and imaging agents in virtue of their unique long absorption wavelengths and near-infrared fluorescence emission.[36−38] Particularly, multi-charged phthalocyanine derivatives possessing good water solubility have been considered as excellent candidates

Received: March 2, 2022
Revised: June 19, 2022

Scheme 1. Schematic Illustration of the Formation of the Adaptive Supramolecular Multivalent NP and Its Application for Targeted Dual-Organelle Imaging and an Enhanced Synergistic Photodynamic Effect

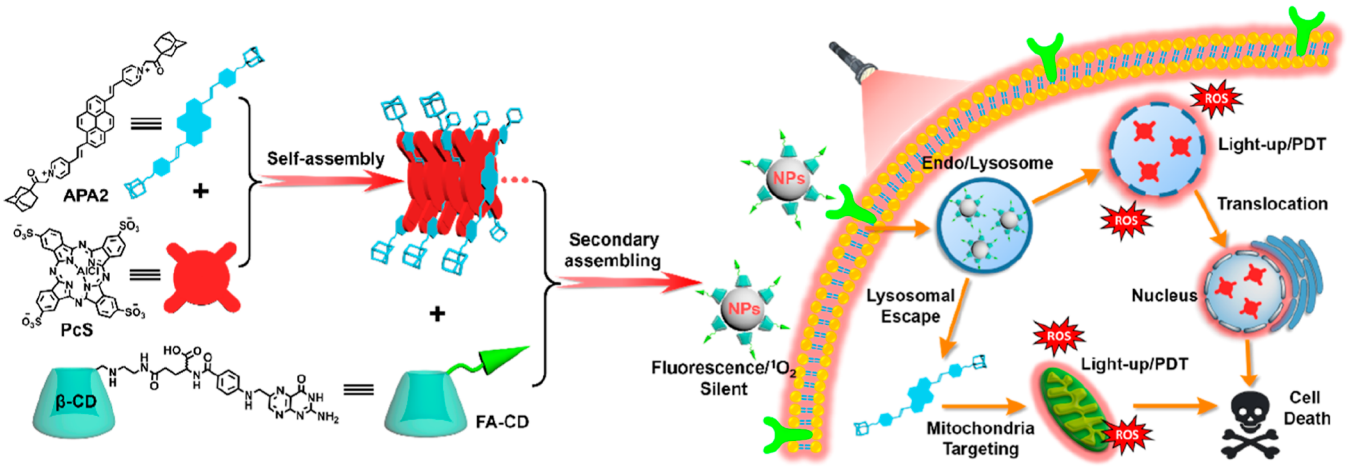

to construct supramolecular dimerization aggregates because they can assemble with themselves or other oppositely charged molecules on account of multiple interactions.[39,40] For example, Yoon and co-workers constructed nucleic-acid-driven activatable nanoassemblies composed of the phthalocyanine photosensitizer and anticancer drug mitoxantrone via a supramolecular strategy and achieved the significantly improved therapeutic effect.[41] Tang and co-workers reported theranostic nanoparticles (NPs) via the self-assembly of sulfonated phthalocyanine and a mitochondria-targeting probe to realize synergistic chemo-PDT.[42] Although the research based on the aggregation process for PDT has made great progress, in situ disassembly of the cyclodextrin-mediated supramolecular multivalent assembly under physiological conditions of cancer cells for targeted dual-organelle imaging and an enhanced synergetic photodynamic effect has rarely been reported.

Herein, we report a novel supramolecular multivalent NP composed of 4,4′-pyrene-1,6-diylbis(ethene-2,1-diyl)bis(1-adamantanylpyridin-1-ium) bromide (APA2), sulfonated aluminum phthalocyanine (PcS), and folic acid-modified β-cyclodextrin (FA−CD) to realize targeted dual-organelle imaging and a cooperative photodynamic effect for high-efficiency cancer cell ablation (Scheme 1). First, a new D−A type photosensitizer APA2 was synthesized via the Knoevenagel condensation. Next, PcS could strongly associate with APA2 in a 1:1 mode to form irregular nanoaggregates due to the multivalent interaction, which was simultaneously accompanied by significant fluorescence quenching and inhibited $^1O_2$ generation. Moreover, FA−CD acting as a target unit was introduced to further co-assemble with PcS/APA2 by virtue of the host−guest interaction between β-cyclodextrin and adamantane to afford homogeneous supramolecular NPs with uniform sizes. Compared with 293T normal cells, thus obtained NPs could be selectively internalized by HeLa cancer cells and could then release photosensitizers at intracellular acidic lysosomes. Subsequently, APA2 and PcS could specifically target mitochondria and lysosomes and then efficiently activate $^1O_2$ generation in situ to cause almost complete cancer cell death under light irradiation. Particularly, it was observed that the released PcS could migrate from the lysosome to the nucleus when cells underwent an apoptosis process under light irradiation, which could be utilized to self-monitor the therapeutic effect within cancer cells in real time.

EXPERIMENTAL SECTION

Synthesis of Compound 2. 1-Adamantyl bromomethyl ketone (515 mg, 2.03 mmol) and 4-methylpyridine (379 mg, 4.06 mmol) were dissolved in anhydrous CH_3CN, and the mixture was heated at reflux for 4 h under a N_2 atmosphere. Then, the solution was evaporated under a reduced pressure. After that, cold diethyl ether was added, and the formed precipitation was filtered. After vacuum-drying, compound 2 (604 mg, 85%) was obtained as a white solid. ^{1}H NMR (400 MHz, DMSO-d_6, ppm): δ 8.72 (d, J = 6.6 Hz, 2H), 8.04 (d, J = 6.4 Hz, 2H), 5.95 (s, 2H), 2.64 (s, 3H), 2.05 (s, 3H), 1.91 (s, 6H), 1.72 (q, J = 12.2 Hz, 6H); ^{13}C NMR (100 MHz, DMSO-d_6, ppm): δ 206.58 (s), 159.98 (s), 145.45 (s), 128.49 (s), 64.64 (s), 45.52 (s), 37.55 (s), 36.32 (s), 27.63 (s), 22.04 (s).

Synthesis of Compound APA2. APA2 was obtained by the Knoevenagel condensation.[43] Pyrene-1,6-dicarbaldehyde 1 (100 mg, 0.39 mmol) and 2 (340 mg, 0.97 mmol) were dissolved in 30 mL of $CHCl_3$ and 10 mL of methanol, and a few drops of piperidine were added. The solution was heated under reflux overnight. After that, the formed precipitate was filtered, washed by diethyl ether and $CHCl_3$, and dried in vacuo to yield APA2 (183 mg, 51%) as a dark red powder. ^{1}H NMR (400 MHz, DMSO-d_6, ppm): δ 9.18 (d, J = 15.7 Hz, 1H), 9.07 (d, J = 9.4 Hz, 1H), 8.80 (d, J = 6.3 Hz, 1H), 8.74 (d, J = 8.2 Hz, 1H), 8.59 (d, J = 6.2 Hz, 1H), 8.52 (d, J = 8.3 Hz, 1H), 8.46 (d, J = 9.5 Hz, 1H), 7.93 (d, J = 15.7 Hz, 1H), 5.92 (s, 1H), 2.09 (s, 1H), 1.96 (s, 2H), 1.75 (q, J = 12.3 Hz, 2H); ^{13}C NMR (100 MHz, DMSO-d_6, ppm): δ 206.09 (s), 145.40 (s), 145.03 (s), 137.03 (s), 136.35 (s), 131.90 (s), 130.02 (s), 129.69 (s), 128.47 (s), 126.23 (s), 124.14 (s), 123.94 (s), 123.90 (s), 63.87 (s), 45.06 (s), 37.08 (s), 35.77 (s), 27.08 (s). HRMS (ESI): m/z calcd for $C_{54}H_{54}N_2O_2^{2+}$, 381.2087 $[M - 2Br^-]^{2+}$; found, 381.2090.

Preparation of NPs. Al(III) phthalocyanine chloride tetrasodium sulfonate (PcS) (4.92 mg, 5 μmol), APA2 (4.61 mg, 5 μmol), and FA−CD (8.0 mg, 5 μmol) were dissolved in deionized water (10 mL), and subsequently, the mixture was ultrasonicated for 30 min. The resulting NP solution was stored at 4 °C for further use.

Cell Culture. The human embryonic kidney normal cell line 293T cells and human cervical carcinoma cancer cell line HeLa cells were all purchased from the Cell Resource Center, Chinese Academy of Medical Science Beijing. HeLa cancer cells and 293T normal cells were cultured with Dulbecco's modified Eagle medium (DMEM) high glucose nutrient medium containing 10% fetal bovine serum (FBS) and 1% penicillin/streptomycin in a humidified incubator with a 5% CO_2 atmosphere at 37 °C. Before being used in experiments, all cells were pre-cultured to achieve confluence.

https://doi.org/10.1021/acs.biomac.2c00276
Biomacromolecules XXXX, XXX, XXX−XXX

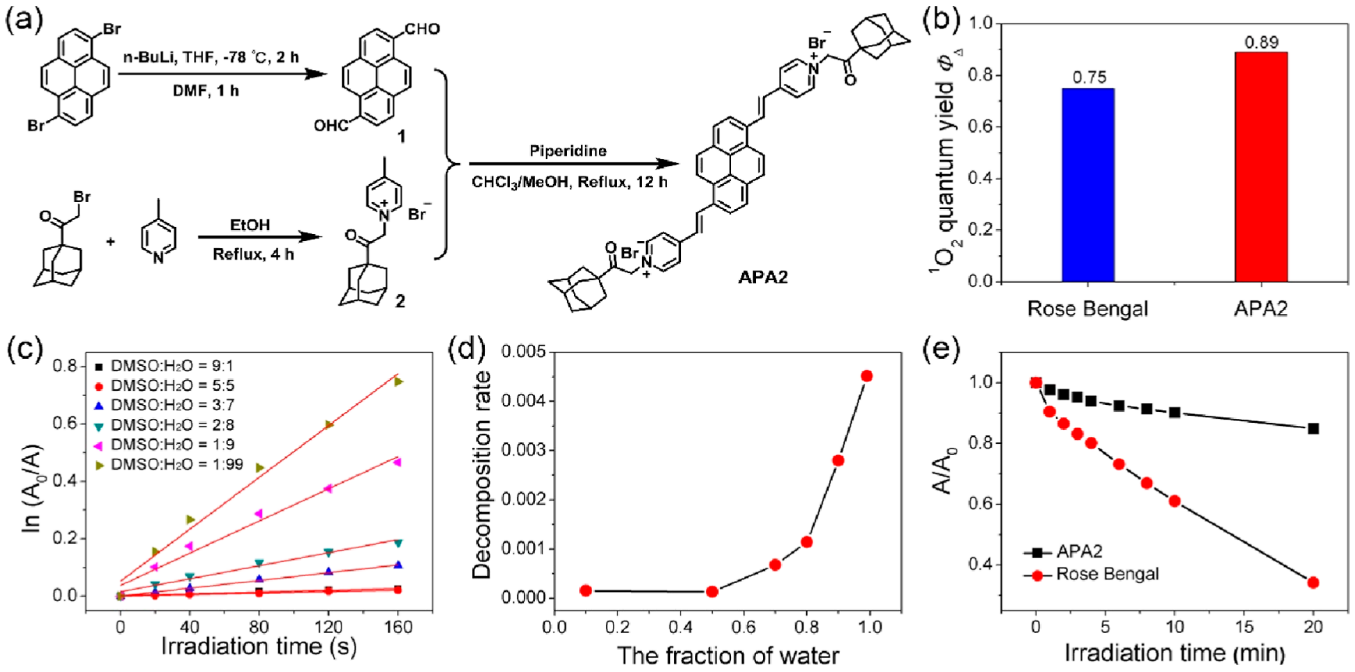

Figure 1. (a) Synthetic route to APA2. (b) $^1O_2$ quantum yield of APA2 with reference to the standard RB in aqueous solution. (c) Absorbance of ABDA at 378 nm in different DMSO/water co-solvents at designated time intervals under the same light irradiation, where A_0 and A represent the absorbances of ABDA before and after light irradiation, respectively. (d) Decomposition rate constants of ABDA by APA2 with the increasing fraction of water. (e) Photostability of APA2 and RB after continuous exposure to light irradiation at different times.

Cellular Uptake Study. HeLa cells and 293T cells were seeded into a confocal Petri dish and cultured for 24 h at 37 °C in a humidified 5% CO_2 atmosphere. HeLa cells were divided into two groups and then incubated with APA2 (5 μM), PcS (5 μM), and NPs ([APA2] = [PcS] = [FA−CD] = 5 μM), and 293T cells were treated with NPs under the same condition. After 24 h of co-incubation, the culture medium was discarded, and the cells were washed with 0.01 M phosphate-buffered saline (PBS) at least three times. Confocal laser scanning microscopy (CLSM) was used to acquire the fluorescence images.

Co-localization Imaging. The co-localization imaging experiments were performed by using commercially available dyes.[44] HeLa cells were first seeded into a confocal Petri dish and incubated for 24 h at 37 °C in a humidified 5% CO_2 atmosphere, then NPs ([APA2] = [PcS] = [FA−CD] = 5 μM) were added into the dish in a culture medium and cultured for another 24 h. After that, the culture medium was discarded, and the cells were washed with 0.01 M PBS at least three times. Next, MitoTracker Green was co-cultured with the cells at 37 °C for 30 min in order to stain mitochondria. After the cells were repeatedly washed with PBS at least three times, the localization in cells was immediately observed by CLSM. The excitation wavelength was set as 488 nm, and the emission was collected in the wavelength range from 510 to 540 nm for MitoTracker Green. The excitation wavelength was set as 488 nm, and the emission was collected in the wavelength range from 650 to 700 nm for APA2. The excitation wavelength was set as 635 nm, and the emission was collected in the wavelength range from 700 to 750 nm for PcS.

Extracellular $^1O_2$ Detection. Commercial 9,10-anthracenediylbis(methylene)dimalonic acid (ABDA) was exploited as a tracer agent to access the differences in $^1O_2$ production efficiencies of different samples. Specifically, each sample and ABDA were together dispersed in 3 mL of deionized water with final concentrations of 0.01 and 0.05 mM, respectively. Then, the mixed solution was irradiated by white light (>420 nm) with a power of 220 mW/cm^2. The $^1O_2$ generation efficiency was measured by monitoring the UV−vis absorbance change of ABDA at 378 nm in different irradiation time intervals.

$^1O_2$ Generation Quantum Yields. Rose Bengal (RB) (Φ_Δ = 0.75 in H_2O) was utilized as the standard, and ABDA was used as an indicator to assess the quantum yields for $^1O_2$ generation of different samples under irradiation.[45] Typically, deionized water solutions with different samples and ABDA (50 μM) were mixed well under dark conditions and then exposed to white light. The absorbance of ABDA at 378 nm were recorded every 20 s. The Φ_Δ values of samples were calculated according to the following formula

$$\Phi_{\Delta(x)} = \Phi_{\Delta(\mathrm{std})} \times \frac{K_x}{K_{\mathrm{std}}} \times \frac{A_{\mathrm{std}}}{A_x}$$

where subscripts std and x, respectively, represent the RB and sample. K indicates the slope of absorbance of ABDA at 378 nm versus irradiation time (s). K_x and K_{std} represent the decomposition rate constants of ABDA by APA2 and RB, respectively. A_{std} and A_x are the integral areas of the absorption spectrum of RB and APA2, respectively.

Intracellular $^1O_2$ Detection. The intracellular $^1O_2$ generation of NPs was studied using a common ROS indicator, 2′,7′-dichlorofluorescin diacetate (DCFH-DA).[46] First, the HeLa cancer cells were co-incubated with a 5 μM concentration of each sample for 24 h. After 24 h of incubation, DCFH-DA was added into the culture medium with incubation for 15 min. Then, the cells were washed with 0.01 M PBS at least three times to remove excess DCFH-DA, and the new culture medium was added, followed by irradiation with white light irradiation for 5 min. Finally, the intracellular $^1O_2$ level was examined immediately by CLSM. The excitation wavelength was set as 488 nm, and the emission wavelength was collected in the range from 500 to 530 nm.

In Vitro Cytotoxicity Tests. First, HeLa cells or 293T cells were plated in 96-well plates and incubated for 24 h. After that, the cells were treated with different concentrations of NPs from 0 to 4 μM for another 24 h in the absence of light. Subsequently, the cells were exposed to white light irradiation (CEL-HXUV300 xenon lamp with a >420 nm cutoff filter at a power density of 220 mW/cm^2) for 5 min. Then, the cells were allowed to continue growing for another 1 h. The culture medium was discarded, and the cells were washed with 0.01 M PBS twice. Then, CCK8 solution was added to each well, and the cells were further incubated at 37 °C for 1 h. The absorbance value was obtained using a microplate reader at 450 nm wavelength. The data

https://doi.org/10.1021/acs.biomac.2c00276
Biomacromolecules XXXX, XXX, XXX−XXX

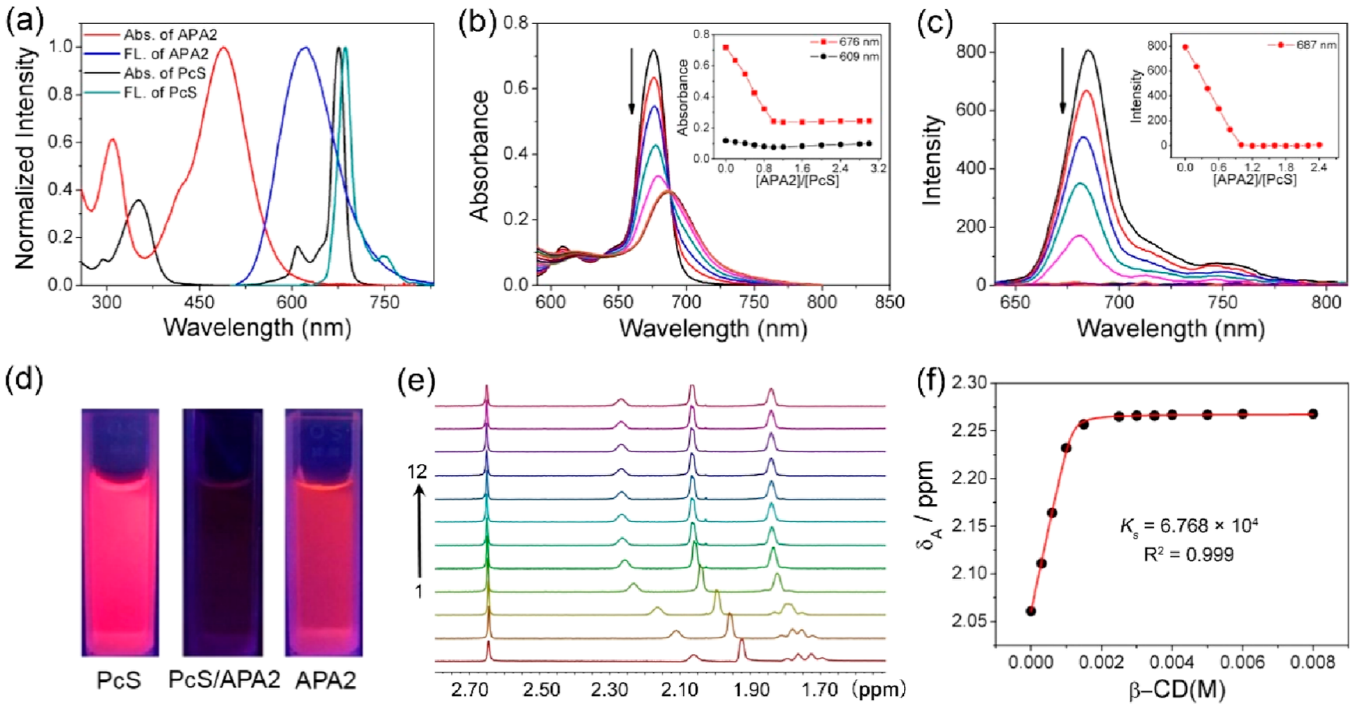

Figure 2. (a) Normalized absorption and emission spectra of APA2 and PcS in aqueous solution. (b) UV−vis spectral changes of PcS (5 μM) upon the addition of 0−3.0 equivalents of APA2 in aqueous solution. Inset: absorbance intensity changes of PcS at 609 and 676 nm. (c) Fluorescence spectral changes of PcS (5 μM) upon the addition of 0−2.4 equivalents of APA2 in aqueous solution. Inset: emission intensity changes of PcS at 687 nm. (d) Photographs of PcS, PcS/APA2, and APA2 under UV light. (e) ^{1}H NMR spectra of model molecule 2 (1 mM) with the addition of 0−8.0 mM β-CD (spectra from 1 to 12) in D_2O at 25 °C. (f) Nonlinear least-squares fit of the chemical shift changes of the two peaks at d = 2.06 ppm as a function of the concentration of β-CD.

were all displayed as the mean ± standard deviation. The NP concentrations were determined on the basis of the photosensitizer. The dark cytotoxicity in vitro was characterized similarly to the phototoxicity characterization described above but without the irradiation. Cell viability was calculated using the following equation

$$\text{Cell viability (\%)} = [(A_s - A_b)/(A_c - A_b)] \times 100\%$$

where A_b is the absorbance of the background and A_s and A_c are the absorbances of solutions with or without samples, respectively.

RESULTS AND DISCUSSION

The synthetic route of APA2 is presented in Figure 1a, where Knoevenagel condensation was conducted between pyrene-1,6-dicarbaldehyde (1) and the adamantyl pyridinium derivative (2) to acquire the target product APA2. APA2 was composed of a pyrene segment as an electron-donating (D) unit, a carbon−carbon double bond as a π-bridge, and pyridinium as an electron-accepting (A) unit. The strong electron donor−acceptor (D−A) interaction within this molecule promoted intramolecular charge transfer, thus leading to longer absorption and emission wavelengths, which made it an excellent candidate for a photosensitizer. First, the $^1O_2$ generation efficiency of APA2 in an aqueous medium was examined by utilizing ABDA as an indicator. Upon white light irradiation for 160 s, the absorption peak of ABDA at 378 nm declined sharply along with irradiation time in the presence of APA2 (Figure S7), and the photodecomposition rate constant was determined to be 5.03 × 10^{-3} S^{-1}, while that of a commercial photosensitizer RB was 3.44 × 10^{-3} S^{-1}. With reference to the standard RB (Φ_Δ = 0.75 in water),[47] the $^1O_2$ quantum yield (Φ_Δ) of APA2 in water was calculated to be 0.89 (Figure 1b), indicating its efficient $^1O_2$ generation performance and great potential for photodynamic application. However, ABDA displayed no apparent decrease in absorption upon mixing with APA2 in a good solvent, dimethyl sulfoxide (DMSO), indicating that APA2 could not produce $^1O_2$ under this experimental condition (Figure S8). Then, the $^1O_2$ generation efficiency of APA2 was studied by tuning its aggregation degree in water/DMSO co-solvents with different volume ratios. As depicted in Figure 1c,d, when water fractions were increased from 1:9 to 99:1 in the mixture of water/DMSO, the photo-decomposition rate constant of ABDA gradually increased (Figure S9), indicating its improved $^1O_2$ generation efficiency, which could be ascribed to the enhanced intersystem crossing effect after aggregation.[48−50] Since existing photosensitizers are susceptible to the photobleaching problem, we also studied the photostability of APA2. After 20 min of white light irradiation, the absorbance of APA2 at its maximum absorption wavelength still remained around 85%, while that of RB decreased to 35%, proving that APA2 had better light stability and photobleaching resistance (Figures 1e and S10).

Subsequently, the binary supramolecular assembly could be conveniently prepared by mixing PcS with APA2 in aqueous solution due to the strong hydrophobic, electrostatic, and $\pi-\pi$ interactions between them. The photophysical behavior associated with the assembly process of PcS and APA2 was examined by UV−vis spectroscopy and fluorescence spectroscopy in detail. The normalized UV−vis absorption spectra and fluorescence spectra of only APA2 and PcS in aqueous solution are presented in Figure 2a. APA2 showed the maximum absorption at 488 nm and an emission centered at 623 nm. Although the emission spectrum of APA2 and the absorption spectrum of PcS had a certain overlap and the florescence

https://doi.org/10.1021/acs.biomac.2c00276
Biomacromolecules XXXX, XXX, XXX−XXX

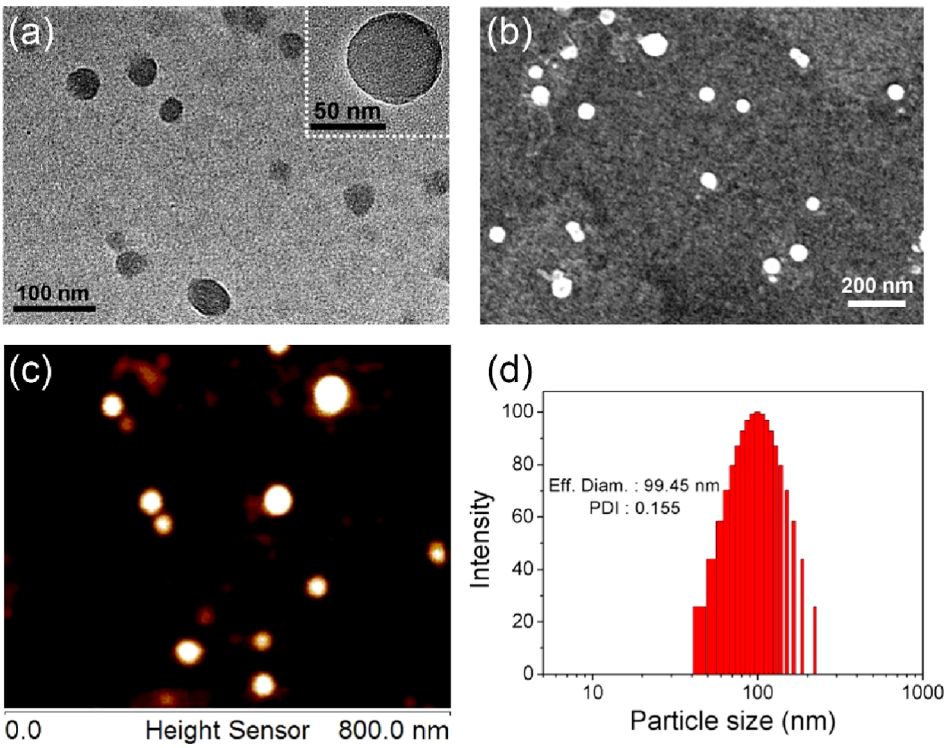

Figure 3. Typical (a) TEM, (b) SEM, and (c) AFM images of NPs and (d) the hydrodynamic diameter of NPs measured by DLS.

resonance energy transfer (FRET) process might occur from APA2 to PcS, both of these two molecules suffered from serious self-quenching after the formation of aggregates, which ultimately resulted in fluorescence quenching of the formed assemblies. As shown in Figure 2b, upon stepwise addition of APA2 into the aqueous solution of PcS, the absorption band of PcS at 676 nm became blunt and its intensity gradually reduced, accompanied by an obvious bathochromic shift from 676 to 686 nm with a clear isosbestic point, implying a transition from free PcS to the PcS/APA2 species. Moreover, the absorbance changes of PcS reached the plateau in the presence of 1.0 equivalent of APA2, indicative of the formation of a stable 1:1 complex between PcS and APA2 (Figure 2b, inset). Similarly, fluorescence intensity of PcS gradually quenched with the stepwise addition of APA2, and a clear inflection point was observed when 1.0 equivalent of APA2 was added, also confirming the 1:1 binding stoichiometry (Figure 2c). In addition, the ζ potential of APA2 alone was 19.0 mV, while the ζ potential of PcS/APA2 was −17.5 mV, further verifying the complexation between PcS and APA2 (Figure S11). It could also be observed that the fluorescence intensity of APA2 underwent a fluorescence quenching process after the stepwise addition of PcS (Figure S12). The photographs taken under UV light (365 nm) through a portable UV lamp provided more intuitive evidence of self-assembly between PcS and APA2. In comparison with free PcS and APA2, which presented brightly fluorescent colors, respectively, a significant fluorescence quenching was found for PcS/APA2 (Figure 2d). In the control experiment, when model molecule 2 without a pyrene core was used to titrate the solution of PcS, neither UV absorption nor fluorescence intensity of PcS showed significant changes, revealing that the pyrene core played an essential role in the self-assembly of PcS and APA2 (Figure S13). The possibly assembled pattern is presented in Scheme 1. These results jointly revealed that PcS could associate with APA2 to form a highly stable heterodimerization complex in aqueous solution favored by the multivalent interactions.

Next, FA−CD was introduced to this binary PcS/APA2 system for further assembly by virtue of the host−guest interaction between cyclodextrin and adamantane to endow the ternary assembly with improved biocompatibility and cancer cell-targeting ability. First, model molecule 2 was utilized as a reference guest and native β-CD was used as a reference host for the ^{1}H NMR titration experiment. As displayed in Figure 2e, the shifted proton signals of adamantane (1.0 mM) shifted downfield gradually from d = 2.06 ppm to d = 2.27 ppm accompanied by shape changes with the increase in the concentration of β-CD from 0 to 8.0 mM, implying the inclusion of adamantane into the cavity of β-CD. Besides, the binding constant (K_s) between adamantane and the β-CD cavity was calculated to be 6.768 × 10^4 M^{-1} by analyzing the nonlinear least-squares fit of the titration data (Figure 2f). In order to determine the optimum proportion of added FA−CD into this binary PcS/APA2 system, a UV−vis titration experiment was carried out. An obvious inflection point appeared after the addition of 1.0 equiv of FA−CD, and the absorption peak of PcS did not change too much at the same time, meaning that the previous binding model could not be destructed (Figure S14). Therefore, the final ternary assembly was obtained by simply adding 1.0 equiv of FA−CD into PcS/APA2 in aqueous solution. Subsequently, high-resolution transmission electron microscopy (HR-TEM), scanning electron microscopy (SEM), atomic force microscopy (AFM), and dynamic light scattering (DLS) experiments were conducted to investigate the direct morphological information of the resultant assemblies. The APA2 alone existed as a discrete spherical morphology with a nanostructure of size about 20 nm, while the binary PcS/APA2 displayed an irregularly cross-linked nanoaggregated structure driven by the strongly multivalent interactions between PcS and APA2

https://doi.org/10.1021/acs.biomac.2c00276
Biomacromolecules XXXX, XXX, XXX−XXX

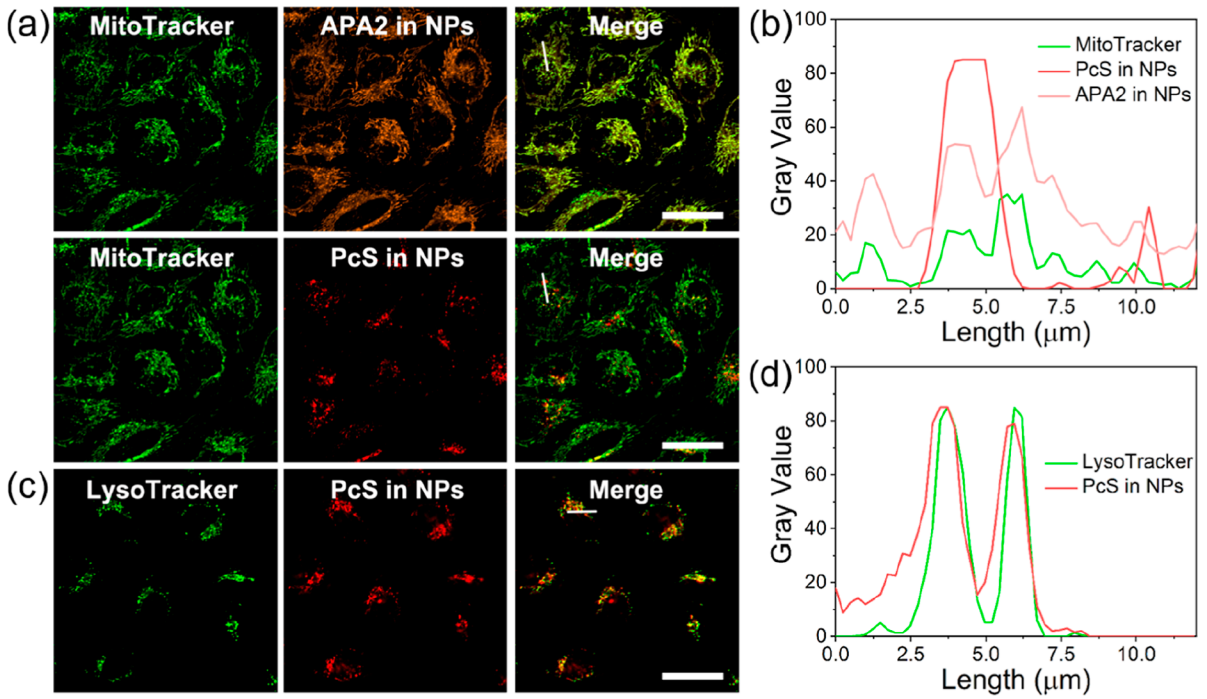

Figure 4. (a) CLSM images of HeLa cells incubated with NPs and MitoTracker. (b) Fluorescence intensity profile of linear ROIs across HeLa cells along the white lines. (c) CLSM images of HeLa cells incubated with NPs and LysoTracker. (d) Fluorescence intensity profile of linear ROIs across HeLa cells along the white lines. For APA2 (yellow channel), λ_{ex} = 488 nm and λ_{em} = 650−700 nm. For PcS (red channel), λ_{ex} = 635 nm and λ_{em} = 700−750 nm. For MitoTracker green and LysoTracker green (Green channel), λ_{ex} = 488 nm and λ_{em} = 510−540 nm. Scale bar = 25 μm.

(Figure S15). The irregular nanoaggregates gradually evolved into a uniform morphology after the addition of 1.0 equiv of FA−CD, which exclusively displayed a number of spherical NPs, and the average diameters of these NPs were around 50 nm on the basis of the TEM analysis (Figures 3a and S16). Moreover, the SEM and AFM images (Figure 3b,c) also gave similar morphological information, which presented many homogeneous spherical NPs with a uniform size. The possible reason for this morphological transformation is that when the adamantane part of such irregular nanoaggregates was encapsulated into the cavity of β-cyclodextrin, the large steric hindrance from the adjacent β-cyclodextrin moieties would result in the twisting of the original nanoaggregates and consequently contribute to the conversion into spherical NPs. In addition, the hydrodynamic diameter of NPs was also measured by DLS to be ca. 99.45 nm with a relatively narrow particle size distribution (Figure 3d). No significant size change was observed when the size distribution of NPs was monitored over the course of 48 h, indicative of the storage stability of NPs (Figure S17). Also, the ζ potential of NPs was measured to be −15.1 mv (Figure S18). In addition, the stability of NPs in neutral and acidic environments was also tested by monitoring the change of the characteristic absorption peak in the UV spectrum. As shown in Figure S19, the absorption band of PcS partially returned to its original sharp state with an intensity increase at the pH = 5.0 condition, indicative of the disassembly of NPs releasing free PcS due to the disruption of the electrostatic interactions.[42] The original spherical NP disintegrated into a shapeless and scattered structure in acidic conditions (Figure S20). The $^1O_2$ generation efficiency was also investigated in these two conditions. Compared with APA2, NPs displayed a reduced efficiency of ABDA decomposition in the neutral condition, signifying the inhibited $^1O_2$ generation, which was probably attributed to the FRET effect from APA2 to PcS. However, the $^1O_2$ generation could be activated in a mildly acidic environment because of the dissociation of PcS/APA2, as indicated by the enhanced ABDA decomposition rate (Figure S21). These results implied that NPs with good sizes would be more conducive to be endocytosed by cancer cells via a receptor-mediated pathway and release free photosensitizers in an intracellular acid environment, which might ensure the highly efficient $^1O_2$ generation.

After fully characterizing these multivalent assemblies NPs, we further investigated their cellular uptake and subcellular localization by using CLSM. Human cervical carcinoma cells (HeLa cancer cells) and human normal embryonic kidney cells (293T normal cells) were chosen as folate receptor-positive cells and folate receptor-negative cells, respectively. As shown in Figure S22, APA2 itself could be specifically distributed in the mitochondria of HeLa cells by co-incubation with commercial MitoTracker Green and exhibit brightly red fluorescence, which overlapped perfectly with that of MitoTracker Green with a high Pearson's correlation coefficient of 0.84, implying the specific mitochondrial targeting ability for APA2 (Figure S23). However, nearly no intracellular fluorescence signal was detected for PcS on account of its strongly negative charges, leading to the poor cell penetrating ability. The absorption spectra of APA2 and PcS hardly overlap according to Figure 2a; therefore, APA2 (λ_{ex} = 488 nm) or PCs (λ_{ex} = 635 nm) can be selectively excited by a specific excitation wavelength. NPs showed different fluorescence distributions under different laser excitations, where the fluorescence signals of both APA2 and PcS could be observed from the CLSM images, indicative of the dissociation of APA2 and PcS (Figure 4a). Moreover, the orange fluorescence signal indicated that APA2 was still strongly colocalized in mitochondria, and the Pearson's correlation

https://doi.org/10.1021/acs.biomac.2c00276
Biomacromolecules XXXX, XXX, XXX−XXX

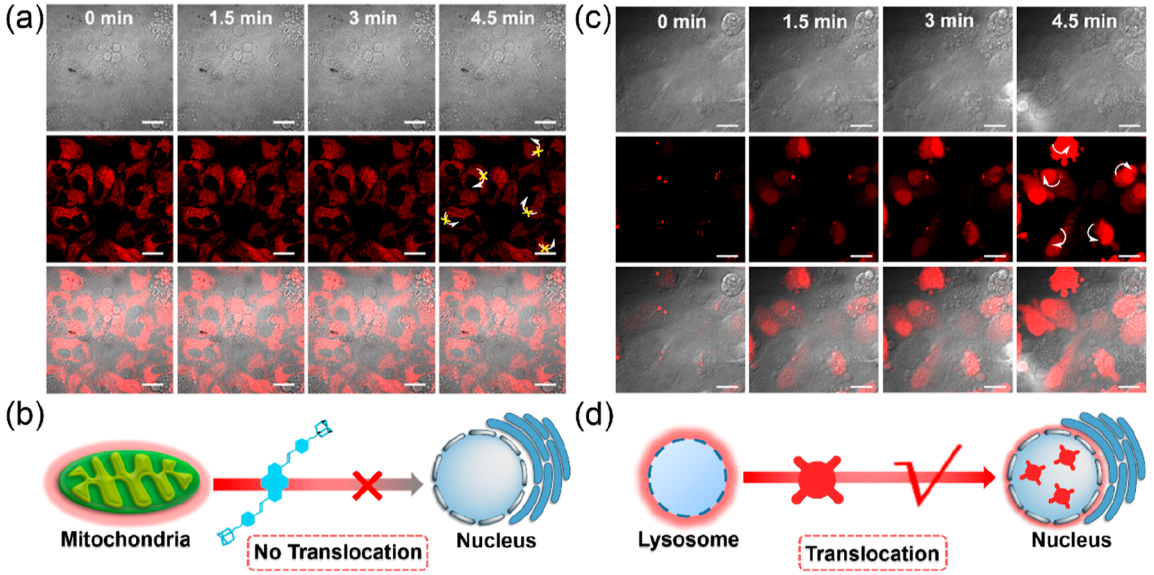

Figure 5. (a) Real-time confocal images of HeLa Cells under continuous 488 nm laser irradiation after incubation with NPs. λ_{ex} = 488 nm and λ_{em} = 650−700 nm. Scale bar = 20 μm. (b) Possible schematics of the translocation process for APA2. (c) Real-time confocal images of HeLa Cells under continuous 635 nm laser irradiation after incubation with NPs. λ_{ex} = 635 nm and λ_{em} = 700−750 nm. (d) Possible schematics of the translocation process for PcS.

coefficient was measured to be 0.85, while the red fluorescence signal derived from PcS indicated poor colocalization in mitochondria with the Pearson's correlation coefficient as low as 0.13 (Figure S24). ROI (linear regions of interest) analysis was also adopted to illustrate the intensity profiles of the co-staining images in Figure 4a, which illustrated that the intensity profiles of MitoTracker green and APA2 tended toward synchronization compared with that of PcS, indicating that APA2 could be site-specifically internalized by the mitochondria (Figure 4b). For further clarifying the targeted organelle of PcS in NPs, a commercial lysosomal dye, LysoTracker green, was also applied to co-stain with NPs (Figure 4c). The intensity profiles of LysoTracker green and PcS tended toward synchronization (Figure 4d). Furthermore, the red fluorescence signal of PcS gave a Pearson's correlation coefficient of 0.78 with LysoTracker green, indicating that PcS derived from NPs could be specifically accumulated in lysosomes (Figure S25). PcS is negatively charged at a neutral pH, which could interact with positively charged APA2, which then further formed NPs after the addition of FA−CD; however, such a process would be reversed in the acidic pH condition. It is well-documented that the lysosome is an acidic organelle (pH 5.0 or lower),[51−53] which may contribute to the disassembly of NPs in such a condition. These phenomena jointly demonstrated that the NPs disaggregated in the acid lysosomes and released free APA2, and this APA2 further escaped from the lysosomes and translocated to the mitochondria, thus together turning on the NIR fluorescence emission. In the control experiment, although PcS/APA2 (no cyclodextrin) can also enter the cells, the degree of their cellular uptake was lower than that of cyclodextrin-stabilized PcS/APA2 and APA2, and NPs showed the most effective cellular uptake capacity by virtue of the folic acid-induced endocytosis, as indicated by the confocal images and flow cytometric analysis (Figures S26 and S27).

More intriguingly, when HeLa cells were incubated with NPs for 12 h and then subjected to confocal laser imaging under 635 nm laser irradiation, it was found that PcS was mainly distributed in the cytoplasm of HeLa cells at the beginning. However, with the extension of laser irradiation time to 1.5 min, the distribution of PcS changed significantly, where the red fluorescence in the cytoplasm weakened while the red fluorescence in the nucleus turned on. Moreover, after 4.5 min of laser irradiation, the nucleus of HeLa cells showed the strongest red fluorescence, and the punctate red fluorescence in the cytoplasm almost disappeared (Figure 5c,d). At the same time, the morphological structure of HeLa cells, including nuclear pyknosis and cell membrane blistering and shrinkage, also changed dramatically in the bright field, all of which were signs of cell apoptosis. In addition, when HeLa cells were irradiated using a continuous 488 nm laser, the phenomenon of cell membrane bubbling could still be observed in the bright field, but the red fluorescence assigned to APA2 displayed a negligible change and was still distributed evenly in the mitochondria under the same experimental conditions (Figure 5a,b). Additionally, compared to that of three other control groups, the apoptosis rate of HeLa cells can reach up to 92.35% when the cells were treated with both NPs and light irradiation, indicative of the most effective cell apoptosis under light (Figure S28). These results illustrated that PcS underwent the process of autonomous translocation from the lysosome to the nucleus during cell apoptosis under 635 nm laser irradiation, but for APA2, similar processes could not occur even under 488 nm laser irradiation, which may be ascribed to the large steric groups in APA2. PcS could not only serve as an excellent photosensitizer under light conditions but also timely monitor the process of apoptosis in situ through the translocation process from the lysosome to the nucleus. The delivery of photosensitizers to the mitochondria and the nuclei of the cancer cells by the translocation process demonstrated the high penetration depth of photosensitizers and contributed to the highly enhanced photosensitization and effective elimination of cancer cells.[16,54,55]

To evaluate the intracellular $^1O_2$ generation of APA2, PcS, and NPs, the commercially available DCFH-DA was utilized as an intracellular ROS indicator. After co-cultivation with these

https://doi.org/10.1021/acs.biomac.2c00276
Biomacromolecules XXXX, XXX, XXX−XXX

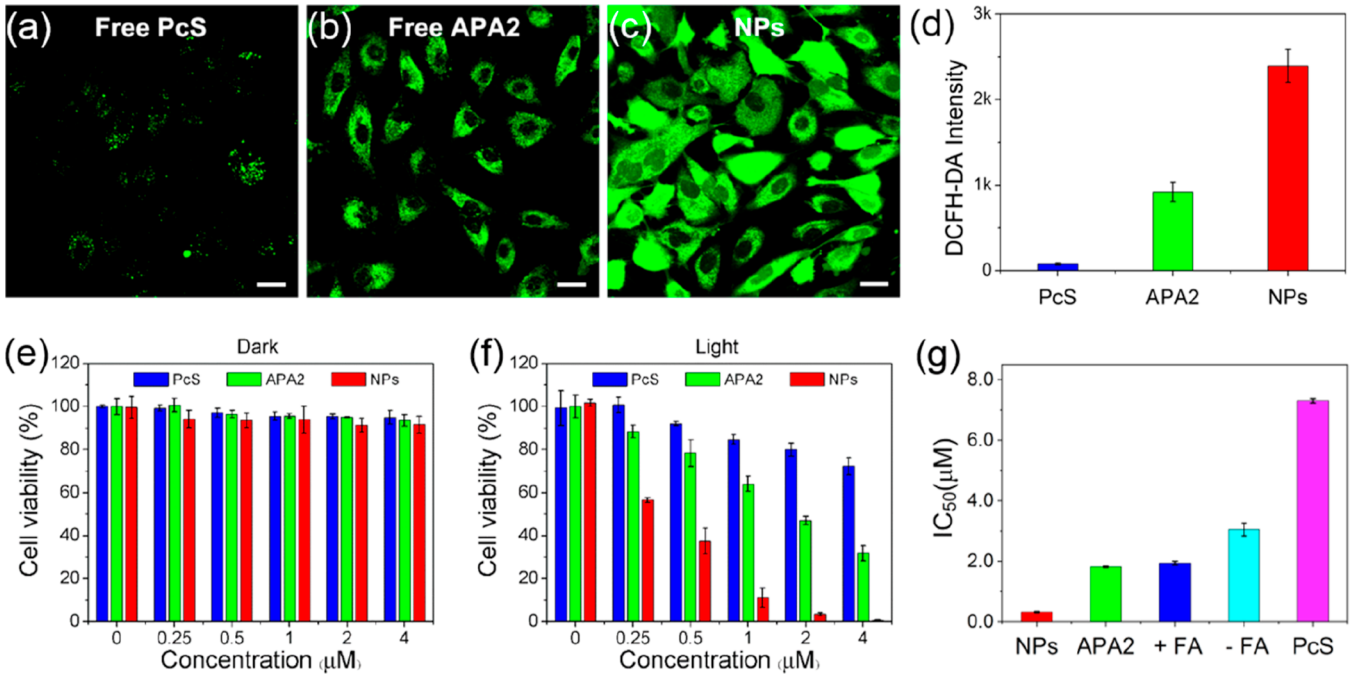

Figure 6. Cellular ROS level imaging by using the DCFH-DA enzyme as an indicator in HeLa cancer cells in the presence of (a) PcS, (b) APA2, and (c) NPs followed by light irradiation for 5 min, respectively. The scale bar is 20 μm. (d) Quantitative fluorescence values of DCFH-DA in HeLa cancer cells. Cell viability of HeLa cancer cells treated with PcS, APA2, and NPs in the dark (e) or after treatment with light irradiation (f) at different concentrations. (g) IC_{50} values of different samples toward HeLa cells.

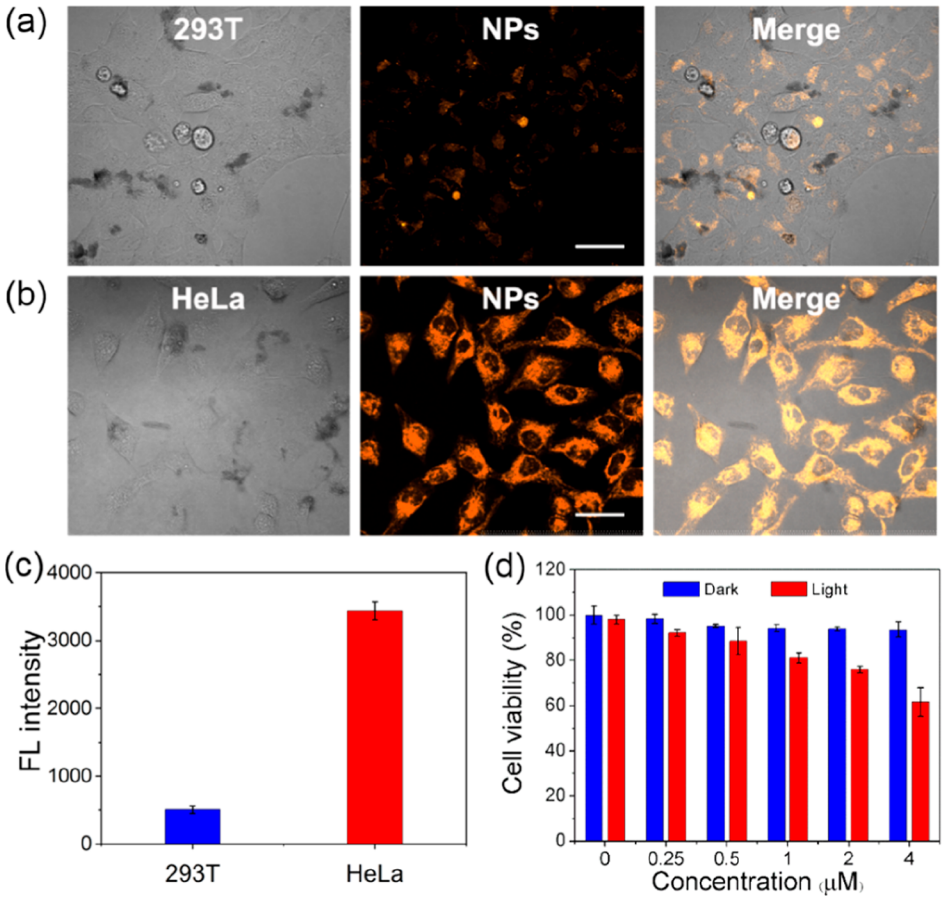

Figure 7. Confocal images of (a) 293T normal cells and (b) HeLa cancer cells incubated with NPs under same conditions. For the yellow channel, λ_{ex} = 488 nm and λ_{em} = 650−700 nm. The scale bar is 40 μm. (c) Quantitative fluorescence values in (a,b). (d) Cell viability of 293T normal cells treated with NPs, followed by treatment with light irradiation or no treatment.

https://doi.org/10.1021/acs.biomac.2c00276
Biomacromolecules XXXX, XXX, XXX−XXX

samples and DCFH-DA followed by subsequent exposure to light, as illustrated in Figure 6a, nearly no green fluorescence was observed in cells treated with PcS. However, intense green fluorescence was detected for cells cultured with APA2, and the NP groups presented the brightest green fluorescence signal, verifying the most efficient intracellular $^1O_2$ generation (Figure 6b,c). Moreover, quantitative analysis of the fluorescence intensity also showed that the intracellular fluorescence intensity arising from NPs under light irradiation was around 2.6 times and 30.3 stronger than that of APA2 and PcS, respectively, implying that the highest intracellular singlet oxygen $^1O_2$ level was produced from decomposed NPs (Figure 6d). In addition, the cells after treatments with PcS/APA2 (no cyclodextrin) or cyclodextrin-stabilized PcS/APA2 can also generate ROS upon irradiation, but their cellular ROS levels were lower that of NPs (Figure S29).

In order to investigate the PDT effects of APA2, PcS, and NPs, the cytotoxicity experiments were carried out in HeLa cancer cells and 293T normal cells. A standard cell counting kit-8 (CCK-8) assay was used to evaluate the cytotoxicity of different samples. As shown in Figure 6e, no obvious cytotoxicity was observed in HeLa cells after incubation with these samples for 24 h at 4 μM, and the cell viability was more than 90%, implying its low cytotoxicity in the dark. Conversely, all of them exhibited malignant cell inhibition effects toward HeLa cells after light irradiation for 5 min (Figure 6f). However, the viability of HeLa cells treated with PcS and light irradiation only decreased to 73% owing to its poor cellular uptake capacity, while APA2 induced higher cytotoxicity under the same conditions with 68% inhibition of tumor cell proliferation. Importantly, the treatment with NPs followed by light irradiation displayed the most dramatically substantial suppression on cell viability. Almost complete cell death was initiated, and the viability of HeLa cells dropped sharply to 0.46% when the concentration of NPs reached 4 μM, suggesting the significant synergistic anticancer effect of NPs. However, the cancer cell inhibition effect of NPs was significantly reduced and the cellular viability was determined to be 45.5% when the receptors on the surface of HeLa cells were blocked by an excess amount of folic acid (Figure S30a). Meanwhile, the binary assemblies PcS/APA2, which had a lack of the targeting agent folic acid, also displayed a remarkably decreased cell inhibition effect with the cellular viability being 46.8% (Figure S30b). Moreover, the corresponding half-maximal inhibitory concentration (IC_{50}) values of NPs, APA2, the FA-treated group, PcS/APA2, and free PcS were measured to be 0.32, 1.81, 1.94, 3.05, and 7.30 μM, respectively (Figure 6g). Notably, APA2 is more potent than PcS/APA2, which could be due to the relatively high cell uptake capacity of APA2 than that of PcS/APA2, which existed as large irregular aggregates not conducive to cell uptake. These results further confirmed the uniform morphology with a suitable size mediated by FA−CD, and the interaction between folic acid and folate receptors played critical roles in the internalization of NPs into cancer cells. Significantly, the killing efficiency of cancer cells could be substantially improved through the synergistic effect of these three components in NPs by targeted PDT.

On the other hand, only HeLa cancer cells exhibited a bright orange fluorescence after treatment with NPs. In contrast, 293T normal cells exhibited ignorable fluorescence, resulting from the poor folic receptors expressed on the cellular surface (Figure 7a,b). The targeting ability of NPs was further verified by fluorescence quantitative analysis of the cells. The 293T normal cells showed fairly low fluorescence intensity, while the HeLa cancer cells exhibited approximately fluorescence 7-fold higher than that of normal cells (Figure 7c), which demonstrated that the resulting ternary assemblies NPs could be selectively internalized by HeLa cells owing to the specific recognition between folic acid and folate receptors, while this receptor-mediated endocytosis was impeded in 293T cells due to the lack of folic acid receptors. NPs also exhibited neglectable toxicity toward 293T cells after incubation for 24 h, implying the good biocompatibility of the supramolecular assemblies in the dark. Moreover, the NPs exhibited a relatively low cytotoxicity toward 293T normal cells than toward HeLa cancer cells upon exposure to white light. The viability of 293T cells still remained at 65% at 4 μM after the light treatment (Figure 7d). These results jointly indicated that the folic acid moiety in NPs could facilitate the cellular uptake of NPs on account of the strong affinity between folic acid and the folate receptor on cancer cells, which not only enhanced the photodynamic therapeutic efficiency toward cancer cells but also reduced the uptake by normal cells and achieved lower side effects.

CONCLUSIONS

In conclusion, a supramolecular multivalent NP has been successfully constructed by combining APA2, PcS, and FA−CD, which existed as homogeneous spherical NPs. Targeted cellular imaging revealed that the obtained well-defined NPs could be specifically taken up by HeLa cancer cells in contrast with 293T normal cells and then decomposed to release free photosensitizers at intracellular acidic lysosomes. Subsequently, APA2 and PcS selectively targeted mitochondria and lysosomes with light-up of near-infrared imaging, which further promoted the efficient singlet oxygen generation and showed a highly effective synergistic photodynamic effect. In vitro cytotoxicity tests demonstrated that NPs caused almost complete HeLa cell death upon light irradiation with the IC_{50} value being as low as 0.32 μM, which was only about one-sixth that of APA2 alone. More strikingly, PcS underwent migration from lysosomes to nuclei under light irradiation, and the nuclei were lit up synchronously, which could be utilized to monitor the death of cancer cells in real time. This study not only expands the application of multivalent assembly mediated by macrocyclic compounds but also offers a new method for specific light-up dual-organelle imaging and highly effective photodynamic cancer cell ablation and holds great promise for the future development of cancer treatment.

ASSOCIATED CONTENT

Supporting Information

The Supporting Information is available free of charge at https://pubs.acs.org/doi/10.1021/acs.biomac.2c00276.

Synthesis procedures of compounds, ^1H NMR and ^{13}C NMR spectra and electrospray ionization mass spectroscopy spectra of compounds, UV−vis absorption spectra and fluorescence spectra, ζ potential results, TEM images, Pearson correlation coefficients, CLSM images, and cell viability tests (PDF)

https://doi.org/10.1021/acs.biomac.2c00276
Biomacromolecules XXXX, XXX, XXX−XXX

AUTHOR INFORMATION

Corresponding Author

Yu Liu − *College of Chemistry, State Key Laboratory of Elemento-Organic Chemistry, Nankai University, Tianjin 300071, China*; orcid.org/0000-0001-8723-1896; Email: yuliu@nankai.edu.cn

Authors

Xianyin Dai − *College of Chemistry, State Key Laboratory of Elemento-Organic Chemistry, Nankai University, Tianjin 300071, China*

Man Huo − *College of Chemistry, State Key Laboratory of Elemento-Organic Chemistry, Nankai University, Tianjin 300071, China*

Bing Zhang − *Department of Biochemistry and Molecular Biology, Key Laboratory of Immune Microenvironment and Disease (Ministry of Education), School of Basic Medical Sciences, Tianjin Medical University, Tianjin 300071, P. R. China*

Zhixue Liu − *College of Chemistry, State Key Laboratory of Elemento-Organic Chemistry, Nankai University, Tianjin 300071, China*

Complete contact information is available at: https://pubs.acs.org/10.1021/acs.biomac.2c00276

Notes

The authors declare no competing financial interest.

ACKNOWLEDGMENTS

This work was financially supported by the National Natural Science Foundation of China (grant no. 22131008).

REFERENCES

(1) Chen, X. M.; Cao, Q.; Bisoyi, H. K.; Wang, M.; Yang, H.; Li, Q. An Efficient Near-Infrared Emissive Artificial Supramolecular Light-Harvesting System for Imaging in the Golgi Apparatus. *Angew. Chem., Int. Ed.* **2020**, *59*, 10493−10497.

(2) Yu, H.-J.; Zhou, Q.; Dai, X.; Shen, F.-F.; Zhang, Y.-M.; Xu, X.; Liu, Y. Photooxidation-Driven Purely Organic Room-Temperature Phosphorescent Lysosome-Targeted Imaging. *J. Am. Chem. Soc.* **2021**, *143*, 13887−13894.

(3) Ma, Y.-L.; Sun, C.; Li, Z.; Wang, Z.; Wei, J.; Cheng, Q.; Zheng, L.-S.; Chang, X.-Y.; Li, K.; Wang, R.; Jiang, W. Biomimetic Recognition-Based Bioorthogonal Host−Guest Pairs for Cell Targeting and Tissue Imaging in Living Animals. *CCS Chem.* **2022**, *4*, 1977−1989.

(4) Liu, Z.; Sun, X.; Dai, X.; Li, J.; Li, P.; Liu, Y. Sulfonatocalix[4]arene-based light-harvesting amphiphilic supramolecular assemblies for sensing sulfites in cells. *J. Mater. Chem. C* **2021**, *9*, 1958−1965.

(5) Zhao, Y.; Huang, Y.; Zhu, H.; Zhu, Q.; Xia, Y. Three-in-One: Sensing, Self-Assembly, and Cascade Catalysis of Cyclodextrin Modified Gold Nanoparticles. *J. Am. Chem. Soc.* **2016**, *138*, 16645−16654.

(6) Yang, K.; Yu, G.; Yang, Z.; Yue, L.; Zhang, X.; Sun, C.; Wei, J.; Rao, L.; Chen, X.; Wang, R. Supramolecular Polymerization-Induced Nanoassemblies for Self-Augmented Cascade Chemotherapy and Chemodynamic Therapy of Tumor. *Angew. Chem., Int. Ed.* **2021**, *60*, 17570−17578.

(7) He, J.; Chen, J.; Lin, S.; Niu, D.; Hao, J.; Jia, X.; Li, N.; Gu, J.; Li, Y.; Shi, J. Synthesis of a Pillar[5]arene-Based Polyrotaxane for Enhancing the Drug Loading Capacity of PCL-Based Supramolecular Amphiphile as an Excellent Drug Delivery Platform. *Biomacromolecules* **2018**, *19*, 2923−2930.

(8) Hu, Y. X.; Li, W. J.; Jia, P. P.; Wang, X. Q.; Xu, L.; Yang, H. B. Supramolecular Artificial Light-Harvesting Systems with Aggregation-Induced Emission. *Adv. Opt. Mater.* **2020**, *8*, 2000265.

(9) Wang, X. H.; Song, N.; Hou, W.; Wang, C. Y.; Wang, Y.; Tang, J.; Yang, Y. W. Efficient Aggregation-Induced Emission Manipulated by Polymer Host Materials. *Adv. Mater.* **2019**, *31*, 1903962.

(10) Lou, X.-Y.; Yang, Y.-W. Manipulating Aggregation-Induced Emission with Supramolecular Macrocycles. *Adv. Opt. Mater.* **2018**, *6*, 1800668.

(11) Fu, S.; Su, X.; Li, M.; Song, S.; Wang, L.; Wang, D.; Tang, B. Z. Controllable and Diversiform Topological Morphologies of Self-Assembling Supra-Amphiphiles with Aggregation-Induced Emission Characteristics for Mimicking Light-Harvesting Antenna. *Adv. Sci.* **2020**, *7*, 2001909.

(12) Hao, M.; Sun, G.; Zuo, M.; Xu, Z.; Chen, Y.; Hu, X. Y.; Wang, L. A Supramolecular Artificial Light-Harvesting System with Two-Step Sequential Energy Transfer for Photochemical Catalysis. *Angew. Chem., Int. Ed.* **2019**, *59*, 10095−10100.

(13) Li, J. J.; Zhang, H. Y.; Liu, G.; Dai, X.; Chen, L.; Liu, Y. Photocontrolled Light-Harvesting Supramolecular Assembly Based on Aggregation-Induced Excimer Emission. *Adv. Opt. Mater.* **2020**, *9*, 2001702.

(14) Chen, H.; Zeng, X.; Tham, H. P.; Phua, S. Z. F.; Cheng, W.; Zeng, W.; Shi, H.; Mei, L.; Zhao, Y. NIR-Light-Activated Combination Therapy with a Precise Ratio of Photosensitizer and Prodrug Using a Host-Guest Strategy. *Angew. Chem., Int. Ed.* **2019**, *58*, 7641−7646.

(15) Huang, B.; Wang, P.; Ouyang, Y.; Pang, R.; Liu, S.; Hong, C.; Ma, S.; Gao, Y.; Tian, J.; Zhang, W. Pillar[5]arene-Based Switched Supramolecular Photosensitizer for Self-Amplified and pH-Activated Photodynamic Therapy. *ACS Appl. Mater. Interfaces* **2020**, *12*, 41038−41046.

(16) Feng, H.-T.; Li, Y.; Duan, X.; Wang, X.; Qi, C.; Lam, J. W. Y.; Ding, D.; Tang, B. Z. Substitution Activated Precise Phototheranostics through Supramolecular Assembly of AIEgen and Calixarene. *J. Am. Chem. Soc.* **2020**, *142*, 15966−15974.

(17) Tian, J.; Xia, L.; Wu, J.; Huang, B.; Cao, H.; Zhang, W. Linear Alternating Supramolecular Photosensitizer for Enhanced Photodynamic Therapy. *ACS Appl. Mater. Interfaces* **2020**, *12*, 32352−32359.

(18) Dai, X.; Zhang, B.; Zhou, W.; Liu, Y. High-Efficiency Synergistic Effect of Supramolecular Nanoparticles Based on Cyclodextrin Prodrug on Cancer Therapy. *Biomacromolecules* **2020**, *21*, 4998−5007.

(19) Zhu, H.; Wang, H.; Shi, B.; Shangguan, L.; Tong, W.; Yu, G.; Mao, Z.; Huang, F. Supramolecular peptide constructed by molecular Lego allowing programmable self-assembly for photodynamic therapy. *Nat. Commun.* **2019**, *10*, 2412.

(20) Chao, S.; Shen, Z.; Pei, Y.; Lv, Y.; Chen, X.; Ren, J.; Yang, K.; Pei, Z. Pillar[5]arene-based supramolecular photosensitizer for enhanced hypoxic-tumor therapeutic effectiveness. *Chem. Commun.* **2021**, *57*, 7625−7628.

(21) Stricker, L.; Fritz, E.-C.; Peterlechner, M.; Doltsinis, N. L.; Ravoo, B. J. Arylazopyrazoles as Light-Responsive Molecular Switches in Cyclodextrin-Based Supramolecular Systems. *J. Am. Chem. Soc.* **2016**, *138*, 4547−4554.

(22) Cheng, H.-B.; Zhang, Y.-M.; Liu, Y.; Yoon, J. Turn-On Supramolecular Host-Guest Nanosystems as Theranostics for Cancer. *Chem* **2019**, *5*, 553−574.

(23) Liu, Z.; Dai, X.; Sun, Y.; Liu, Y. Organic supramolecular aggregates based on water-soluble cyclodextrins and calixarenes. *Aggregate* **2020**, *1*, 31−44.

(24) Zhou, W.-L.; Zhao, X.; Chen, Y.; Liu, Y. Construction and heterogeneous photooxidization reactivity of a cyclodextrin/porphyrin polyrotaxane network. *Org. Chem. Front.* **2019**, *6*, 10−14.

(25) Zhang, Y.-M.; Zhang, N.-Y.; Xiao, K.; Yu, Q.; Liu, Y. Photo-Controlled Reversible Microtubule Assembly Mediated by Paclitaxel-Modified Cyclodextrin. *Angew. Chem., Int. Ed.* **2018**, *57*, 8649−8653.

(26) Shi, X.; Hou, M.; Ma, X.; Bai, S.; Zhang, T.; Xue, P.; Zhang, X.; Liu, G.; Kang, Y.; Xu, Z. Starburst Diblock Polyprodrugs: Reduction-Responsive Unimolecular Micelles with High Drug Loading and Robust Micellar Stability for Programmed Delivery of Anticancer Drugs. *Biomacromolecules* **2019**, *20*, 1190−1202.
(27) Song, X.; Zhang, Z.; Zhu, J.; Wen, Y.; Zhao, F.; Lei, L.; Phan-Thien, N.; Khoo, B. C.; Li, J. Thermoresponsive Hydrogel Induced by Dual Supramolecular Assemblies and Its Controlled Release Property for Enhanced Anticancer Drug Delivery. *Biomacromolecules* **2020**, *21*, 1516−1527.
(28) Sun, J.; Cai, X.; Wang, C.; Du, K.; Chen, W.; Feng, F.; Wang, S. Cascade Reactions by Nitric Oxide and Hydrogen Radical for Anti-Hypoxia Photodynamic Therapy Using an Activatable Photosensitizer. *J. Am. Chem. Soc.* **2021**, *143*, 868−878.
(29) Tong, H.; Chen, Y.; Li, Z.; Li, H.; Chen, T.; Jin, Q.; Ji, J. Glutathione Activatable Photosensitizer-Conjugated Pseudopolyrotaxane Nanocarriers for Photodynamic Theranostics. *Small* **2016**, *12*, 6223−6232.
(30) Zhang, Z.; Wang, R.; Luo, R.; Zhu, J.; Huang, X.; Liu, W.; Liu, F.; Feng, F.; Qu, W. An Activatable Theranostic Nanoprobe for Dual-Modal Imaging-Guided Photodynamic Therapy with Self-Reporting of Sensitizer Activation and Therapeutic Effect. *ACS Nano* **2021**, *15*, 5366−5383.
(31) Zhang, Y.-H.; Li, X.; Huang, L.; Kim, H. S.; An, J.; Lan, M.; Cao, Q.-Y.; Kim, J. S. AIE based GSH activatable photosensitizer for imaging-guided photodynamic therapy. *Chem. Commun.* **2020**, *56*, 10317−10320.
(32) Hu, D.; Zhong, L.; Wang, M.; Li, H.; Qu, Y.; Liu, Q.; Han, R.; Yuan, L.; Shi, K.; Peng, J.; Qian, Z. Perfluorocarbon-Loaded and Redox-Activatable Photosensitizing Agent with Oxygen Supply for Enhancement of Fluorescence/Photoacoustic Imaging Guided Tumor Photodynamic Therapy. *Adv. Funct. Mater.* **2019**, *29*, 1806199.
(33) Shao, L.; Pan, Y.; Hua, B.; Xu, S.; Yu, G.; Wang, M.; Liu, B.; Huang, F. Constructing Adaptive Photosensitizers via Supramolecular Modification Based on Pillararene Host−Guest Interactions. *Angew. Chem., Int. Ed.* **2020**, *59*, 11779−11783.
(34) Mei, J.; Leung, N. L. C.; Kwok, R. T. K.; Lam, J. W. Y.; Tang, B. Z. Aggregation-Induced Emission: Together We Shine, United We Soar. *Chem. Rev.* **2015**, *115*, 11718−11940.
(35) Li, J.; Wang, J.; Li, H.; Song, N.; Wang, D.; Tang, B. Z. Supramolecular materials based on AIE luminogens (AIEgens): construction and applications. *Chem. Soc. Rev.* **2020**, *49*, 1144−1172.
(36) Li, X.; Lee, S.; Yoon, J. Supramolecular photosensitizers rejuvenate photodynamic therapy. *Chem. Soc. Rev.* **2018**, *47*, 1174−1188.
(37) Li, D.; Wang, X.-Z.; Yang, L.-F.; Li, S.-C.; Hu, Q.-Y.; Li, X.; Zheng, B.-Y.; Ke, M.-R.; Huang, J.-D. Size-Tunable Targeting-Triggered Nanophotosensitizers Based on Self-Assembly of a Phthalocyanine−Biotin Conjugate for Photodynamic Therapy. *ACS Appl. Mater. Interfaces* **2019**, *11*, 36435−36443.
(38) Lo, P.-C.; Rodríguez-Morgade, M. S.; Pandey, R. K.; Ng, D. K. P.; Torres, T.; Dumoulin, F. The unique features and promises of phthalocyanines as advanced photosensitisers for photodynamic therapy of cancer. *Chem. Soc. Rev.* **2020**, *49*, 1041−1056.
(39) Li, X.; Yu, S.; Lee, Y.; Guo, T.; Kwon, N.; Lee, D.; Yeom, S. C.; Cho, Y.; Kim, G.; Huang, J.-D.; Choi, S.; Nam, K. T.; Yoon, J. In Vivo Albumin Traps Photosensitizer Monomers from Self-Assembled Phthalocyanine Nanovesicles: A Facile and Switchable Theranostic Approach. *J. Am. Chem. Soc.* **2018**, *141*, 1366−1372.
(40) Li, X.; Park, E. Y.; Kang, Y.; Kwon, N.; Yang, M.; Lee, S.; Kim, W. J.; Kim, C.; Yoon, J. Supramolecular Phthalocyanine Assemblies for Improved Photoacoustic Imaging and Photothermal Therapy. *Angew. Chem., Int. Ed.* **2020**, *59*, 8630−8634.
(41) Li, X.; Yu, S.; Lee, D.; Kim, G.; Lee, B.; Cho, Y.; Zheng, B.-Y.; Ke, M.-R.; Huang, J.-D.; Nam, K. T.; Chen, X.; Yoon, J. Facile Supramolecular Approach to Nucleic-Acid-Driven Activatable Nanotheranostics That Overcome Drawbacks of Photodynamic Therapy. *ACS Nano* **2017**, *12*, 681−688.
(42) Chen, X.; Li, Y.; Li, S.; Gao, M.; Ren, L.; Tang, B. Z. Mitochondria- and Lysosomes-Targeted Synergistic Chemo-Photodynamic Therapy Associated with Self-Monitoring by Dual Light-Up Fluorescence. *Adv. Funct. Mater.* **2018**, *28*, 1804362.
(43) Li, S.-H.; Xu, X.; Zhou, Y.; Zhao, Q.; Liu, Y. Reversibly Tunable White-Light Emissions of Styrylpyridiniums with Cucurbiturils in Aqueous Solution. *Org. Lett.* **2017**, *19*, 6650−6653.
(44) Xu, W.; Lee, M. M. S.; Nie, J. J.; Zhang, Z.; Kwok, R. T. K.; Lam, J. W. Y.; Xu, F. J.; Wang, D.; Tang, B. Z. Three-Pronged Attack by Homologous Far-red/NIR AIEgens to Achieve 1 + 1 + 1 > 3 Synergistic Enhanced Photodynamic Therapy. *Angew. Chem., Int. Ed.* **2020**, *59*, 9610−9616.
(45) Zhang, T.; Li, Y.; Zheng, Z.; Ye, R.; Zhang, Y.; Kwok, R. T. K.; Lam, J. W. Y.; Tang, B. Z. In Situ Monitoring Apoptosis Process by a Self-Reporting Photosensitizer. *J. Am. Chem. Soc.* **2019**, *141*, 5612−5616.
(46) Li, M.; Long, S.; Kang, Y.; Guo, L.; Wang, J.; Fan, J.; Du, J.; Peng, X. De Novo Design of Phototheranostic Sensitizers Based on Structure-Inherent Targeting for Enhanced Cancer Ablation. *J. Am. Chem. Soc.* **2018**, *140*, 15820−15826.
(47) Chen, Y.; Ai, W.; Guo, X.; Li, Y.; Ma, Y.; Chen, L.; Zhang, H.; Wang, T.; Zhang, X.; Wang, Z. Mitochondria-Targeted Polydopamine Nanocomposite with AIE Photosensitizer for Image-Guided Photodynamic and Photothermal Tumor Ablation. *Small* **2019**, *15*, 1902352.
(48) Lee, E.; Li, X.; Oh, J.; Kwon, N.; Kim, G.; Kim, D.; Yoon, J. A boronic acid-functionalized phthalocyanine with an aggregation-enhanced photodynamic effect for combating antibiotic-resistant bacteria. *Chem. Sci.* **2020**, *11*, 5735−5739.
(49) Yang, L.; Wang, X.; Zhang, G.; Chen, X.; Zhang, G.; Jiang, J. Aggregation-induced intersystem crossing: a novel strategy for efficient molecular phosphorescence. *Nanoscale* **2016**, *8*, 17422−17426.
(50) Ji, C.; Gao, Q.; Dong, X.; Yin, W.; Gu, Z.; Gan, Z.; Zhao, Y.; Yin, M. A Size-Reducible Nanodrug with an Aggregation-Enhanced Photodynamic Effect for Deep Chemo-Photodynamic Therapy. *Angew. Chem., Int. Ed.* **2018**, *57*, 11384−11388.
(51) Li, Y.; Wu, Q.; Li, D.; Huang, J.; Wen, H.; Wu, Y.; Wang, D.; Tang, B. Z. A Nanotheranostic System Combining Lysosomal Cell Death and Nuclear Apoptosis Functions for Synergistic Cancer Therapy and Addressing Drug Resistance. *Adv. Funct. Mater.* **2021**, *31*, 2106091.
(52) Roy, I.; Bobbala, S.; Young, R. M.; Beldjoudi, Y.; Nguyen, M. T.; Cetin, M. M.; Cooper, J. A.; Allen, S.; Anamimoghadam, O.; Scott, E. A.; Wasielewski, M. R.; Stoddart, J. F. A Supramolecular Approach for Modulated Photoprotection, Lysosomal Delivery, and Photodynamic Activity of a Photosensitizer. *J. Am. Chem. Soc.* **2019**, *141*, 12296−12304.
(53) Zhang, Y.; Zhao, R.; Liu, J.; Kong, H.; Zhang, K.; Zhang, Y.-N.; Kong, X.; Zhang, Q.; Zhao, Y. Hierarchical nano-to-molecular disassembly of boron dipyrromethene nanoparticles for enhanced tumor penetration and activatable photodynamic therapy. *Biomaterials* **2021**, *275*, 120945.
(54) Wang, R.; Li, X.; Yoon, J. Organelle-Targeted Photosensitizers for Precision Photodynamic Therapy. *ACS Appl. Mater. Interfaces* **2021**, *13*, 19543−19571.
(55) Xiao, B.; Wang, Q.; Zhang, S.; Li, X.-Y.; Long, S.-Q.; Xiao, Y.; Xiao, S.; Ni, X.-L. Cucurbit[7]uril-anchored polymer vesicles enhance photosensitization in the nucleus. *J. Mater. Chem. B* **2019**, *7*, 5966−5971.

https://doi.org/10.1021/acs.biomac.2c00276
Biomacromolecules XXXX, XXX, XXX−XXX